

Abelian and non-abelian symmetries in infinite projected entangled pair states

Claudius Hubig

Max-Planck-Institut für Quantenoptik,
Hans-Kopfermann-Str. 1, 85748 Garching, Germany
claudius.hubig@mpq.mpg.de

17th October 2018

Abstract

We explore in detail the implementation of arbitrary abelian and non-abelian symmetries in the setting of infinite projected entangled pair states on the two-dimensional square lattice. We observe a large computational speed-up; easily allowing bond dimensions $D = 10$ in the square lattice Heisenberg model at computational effort comparable to calculations at $D = 6$ without symmetries. We also find that implementing an unbroken symmetry does not negatively affect the representative power of the state and leads to identical or improved ground-state energies. Finally, we point out how to use symmetry implementations to detect spontaneous symmetry breaking.

1 Introduction

Tensor network methods have become the de facto method of choice in the numerical treatment of one-dimensional quantum systems [1]. The extension to other loop-free geometries is relatively straightforward [2–7] and preserves most of the numerical advantages of the one-dimensional systems. Work is still ongoing, however, to effectively and efficiently handle large two-dimensional systems which are firstly both of extremely high experimental and theoretical interest and secondly difficult to treat numerically with any method. For example, the dynamical mean-field theory is being combined with new and different solvers [7–9] to allow the treatment of larger clusters within the dynamical cluster approximation; a similar approach is taken for the density matrix embedding theory [10, 11] to likewise allow for larger clusters [12] potentially necessary for the treatment of two-dimensional lattices. Recently, a diagrammatic formulation of quantum Monte Carlo [13] was also used to further avoid the sign problem, which otherwise makes calculations in frustrated or fermionic systems very hard. Standard matrix-product state/density-matrix renormalisation group (MPS-DMRG) methods are also continuously applied to wider and wider cylinders, but computational costs essentially explode beyond relatively limited cylinder circumferences [14–17].

Projected entangled pair states [18], the two-dimensional generalisation of matrix-product states, were proposed soon after the understanding of the latter in the context of the density matrix renormalisation group and a further generalisation to *infinite* two-dimensional systems [19, 20] followed with continuous improvements [21–29] to the method over the last few years. In this work, we explore the implementation of both abelian and non-abelian symmetries – which is a standard method in one-dimensional MPS codes – with the infinite projected

entangled pair states (iPEPS) method used to calculate two-dimensional ground-state properties. In particular, we will show that, absent spontaneous symmetry breaking, implementing an abelian or non-abelian symmetry provides a major computational advantage and considerably improved estimates for the ground-state energy. This will be done using the explicit Clebsch-Gordan Coefficients approach introduced in Ref. [30]. Furthermore, we will showcase how the implementation of a symmetry allows additional control over a calculation: First, once the symmetry is implemented, one forces the calculation into a canonical ensemble, hence exactly preserving e.g. particle number at the desired and manually-selected value. Second, enabling or disabling the preservation of the symmetry allows selecting between symmetry-unbroken and symmetry-broken states and phases. By comparing the energies of these states, it becomes very easy and very stable to pinpoint phase transitions.

To this end, the paper is structured as follows: Sec. 2 reviews the implementation of arbitrary symmetries in tensor networks and establishes some notation. Sec. 3 goes into further detail of required adaptations of the standard iPEPS algorithms to allow for such an implementation as well as different considerations of computational effort. In Sec. 4, we use the Heisenberg $S = 1/2$ Hamiltonian on a square and Kagomé lattice to show the computational speed-up attainable by implementing symmetries in the network. In particular, a large benefit due to the implementation of the unbroken $SU(2)$ -spin symmetry in the Kagomé lattice is observed. The selection of symmetry-broken and symmetry-unbroken states and their use in diagnosing spontaneous symmetry breaking is discussed in Sec. 5. Finally, we conclude in Sec. 6.

2 Symmetries in tensor networks

The implementation of global abelian symmetries in low-rank loop-free tensor networks is generally well-understood and a cornerstone of efficient computations in modern codes [1, 31–33]. In contrast to this, global non-abelian symmetries [34] have seen less widespread use and proposals on how to implement them for higher-rank tensor networks are relatively new [30, 35]. While global abelian symmetries generalise straightforwardly to higher-rank tensors (see e.g. Ref. [36, 37] for applications to (i)PEPS), for non-abelian symmetries there are two alternative approaches: the *implicit Clebsch-Gordan coefficients approach* relies on analytical knowledge of Clebsch-Gordan coefficients (CGCs) for rank-3 tensors and decomposes any higher-rank tensor into a double tree of rank-3 tensors [35, 38]. Alternatively, the *explicit CGC approach* generalises the notion of CGCs to higher-rank tensors and explicitly stores those coefficients within the tensor [30]. The latter approach was already applied to iPEPS calculations in Ref. [39, 40].

Here, we will briefly summarise the implementation of arbitrary symmetries following the *explicit CGC approach* as done in the SYTEN toolkit [41]. For a more extensive discussion of this approach, see Refs. [30, 42]. In Sec. 3 we will then go on to discuss implementation details specific to iPEPS calculations.

Fundamentally, a rank- R tensor T is represented as a direct sum of a finite number of blocks $\{t_i\}$:

$$T = \bigoplus_{i=1}^{N_t} t_i \quad . \quad (1)$$

Each of the R legs of the tensor is given a direction corresponding to the tensor acting on

the vector space on this leg or its dual. A matrix, for example, would have one incoming leg and one outgoing leg. Every block t_i then firstly contains a single quantum number label for every symmetry in the system (e.g. U(1) particle number n and SU(2) spin S) on each of its R legs. Furthermore, each block contains one dense *reduced* rank- R tensor m_i and, for every symmetry γ , a *generalised CGC* rank- R tensor c_i^γ :

$$t_i = m_i \bigotimes_{\gamma=1}^{N_S} c_i^\gamma \quad . \quad (2)$$

Blocks with the same quantum numbers on all legs can be added directly, blocks with different quantum numbers are placed next to each other (cf. Eq. (4)). If there are no symmetries in the system, the tensor T only contains a single block t_1 which, in turn, only contains the collection of scalar coefficients of the tensor. For abelian symmetries, c_i^γ are one-dimensional tensors which are non-zero if the addition rules for the abelian symmetry are fulfilled by the quantum numbers assigned to the tensor legs and zero if the addition rules are broken. Alternatively, the c_i^γ can be left off and the addition rules enforced by hand. For rank-2 tensors with one incoming and one outgoing index, c_i^γ are proportional to identity matrices, for rank-3 tensors, they correspond directly to the standard Clebsch-Gordan coefficients.

As an example, consider a rank-2 tensor T with a single preserved SU(2)-spin symmetry. The blocks of the tensor are labelled by the SU(2)-spin quantum numbers of the states on the incoming and outgoing tensor legs. Let the tensor contain three blocks corresponding to $S = 0$, $S = 1/2$ and $S = 1$:

$$T = t_{0,0} \oplus t_{1/2,1/2} \oplus t_{1,1} \quad . \quad (3)$$

The implicit direct sum is equivalent to placing the three blocks on the diagonal of a larger matrix:

$$T = \begin{pmatrix} [t_{0,0}] & 0 & 0 \\ \cancel{[t_{1/2,0}]} & [t_{1/2,1/2}] & 0 \\ 0 & 0 & [t_{1,1}] \end{pmatrix} \quad . \quad (4)$$

The location of a hypothetical block $t_{1/2,0}$ is also shown but this block (like all other zeros in the T tensor) is forbidden by the symmetry and must be identically zero. The decomposition according to Eq. (2) then allows rewriting each block t_i as the tensor product of a reduced block and a symmetry-protected CGC tensor c_i . Since the tensor T is a rank-2 tensor, the c_i are simply identity matrices of the appropriate size: 1×1 , 2×2 and 3×3 respectively, as the irreducible representations $S = 0$, $S = 1/2$ and $S = 1$ are one-, two- and three-dimensional respectively:

$$t_{0,0} = m_{0,0} \otimes \mathbf{1}_1 \quad (5)$$

$$t_{1/2,1/2} = m_{1/2,1/2} \otimes \mathbf{1}_2 \quad (6)$$

$$t_{1,1} = m_{1,1} \otimes \mathbf{1}_3 \quad . \quad (7)$$

While $t_{0,0}$ and $m_{0,0}$ have exactly the same number of rows and columns, $t_{1/2,1/2}$ has twice the number of rows and columns as $m_{1/2,1/2}$ (and four times the number of elements) while $t_{1,1}$ has nine times as many elements as $m_{1,1}$! This already is an indicator of the power of non-abelian symmetries in tensor networks.

In comparison, an *abelian* symmetry would still allow for the decomposition of the tensor T into blocks. The $S^z = 0$ block $t_{0,0}$, however, would contain contributions from the $S = 0$ and the $S = 1$ sector (and hence would be larger). It would also not be possible to exploit the two-fold degeneracy of the $S = 1/2$ sector, one would instead have to keep two blocks $t_{\pm 1/2}$. In this case, all c_i would be 1×1 dummy matrices.

Note that here we force every tensor to preserve the symmetry exactly and do not allow for a shift of all quantum numbers within a tensor, as such shifts are only well-defined for abelian symmetries and would break down immediately when including non-abelian symmetries.

Tensor operations can then be implemented to largely act independently on each block and also the m_i and c_i^γ within each block. The addition of two tensors $T + S$ is simply a direct sum over all blocks:

$$T + S = \bigoplus_{x=t,s} \bigoplus_{i=1}^{N_x} x_i \quad . \quad (8)$$

However, we may then end up with many blocks with identical quantum numbers on all legs and an identical Clebsch-Gordan structure. If for every symmetry in the system, the associated CGC tensors of two blocks are parallel to each other, we may move those factors into the reduced dense tensors and then add the reduced dense tensors together to arrive at a single block consisting of the sum of the dense tensors as well as one set of CGC tensors. This operation hence reduces the number of blocks in the direct sum and is called a *reduction* in the following (not to be confused with the reduced tensor m_i above).

The contraction of two tensors T and S , $R = T \cdot S$ over a set of legs is evaluated as follows: First, collect all pairs of blocks $\{t_i, s_j\}$ which are labelled by identical quantum numbers on the contracted legs. Then construct result blocks r_k as

$$r_k = (m_{t,i} \cdot m_{s,j}) \bigotimes_{\gamma=1}^{N_s} (c_{t,i}^\gamma \cdot c_{s,j}^\gamma) \quad (9)$$

where \cdot denotes the desired contraction. Afterwards reduce the number of blocks of the result tensor R as described above by adding parallel tensor blocks.

While it is straightforward to parallelise over the pairs of all possible contractions, to reduce memory usage, one should also first collect all contraction pairs resulting in a given quantum number configuration on the open legs, contract and reduce those and only then move on to the next set of quantum numbers on the open legs. Otherwise, the intermediate, unreduced R tensor can easily exceed the size of the actual reduced R by a factor of 100.

Reduced and Total Dimensions When speaking about the *bond dimension* of a tensor network state or more generally the dimensions of a tensor, it is useful to differentiate between the *reduced* and the *total* dimension. Here, the *reduced dimension* of a tensor on one of its legs is the sum of the sizes of every reduced block (counted only once per quantum number sector). In comparison, the *total dimension* of a tensor on one of its legs is the sum of the sizes of every reduced block multiplied by the product of the sizes of the associated generalised CGC tensors. Put another way, a spin doublet state with two duplicate singular values associated to $\pm 1/2$ has a total dimension of two regardless of the symmetries used to represent it. However, if the tensor implements the $SU(2)$ spin symmetry, the *reduced* dimension of the state is merely 1, the duplicate-ness of the singular values is not counted. We then typically expect computational

effort to scale cubically in the reduced dimensions, whereas the expressivity of a tensor and the potentially carried entanglement scales with its total dimensions. To differentiate the two in the following text, we will use capital letters (D , X) to refer to total dimensions whereas lower-case letters (d , χ) refer to the reduced dimensions. In the iPEPS calculations to follow, d and D respectively will denote the state bond dimension whereas χ and X respectively will denote the environment bond dimension.

The distribution of states among the different quantum number sectors is in principle open and should be adapted according to the specific state represented. While at relatively small bond dimensions (as encountered in iPEPS calculations) it may be feasible to fix that distribution by hand beforehand, finding the optimal choice a priori becomes combinatorially expensive. To avoid this problem, minimal care must be taken to allow flexibility in the choice of quantum number sectors. Within the full update scheme with imaginary time evolution, this flexibility comes naturally. For the newer variational update schemes [27, 28] one may have to consider either two-site updates or an expansion scheme analogous to the subspace expansion in DMRG [43].

3 Implementation details specific to iPEPS

Our iPEPS calculation largely follows the existing literature, making use of imaginary time evolution with the fast full update (FFU) [25] and gauge fixing [24, 26]. The corner transfer matrix is truncated as suggested in [23]. During the optimisation, we aim for a total environment bond dimension X approximately ten times the total state bond dimension D .

Errors for observables from the corner transfer matrix method are estimated as follows: First, at given environment bond dimension χ , corner transfer matrix (CTM) steps are done until the observable changes by less than a small threshold (10^{-8}) or 15 steps are done. The first error is then the maximum change between the last three steps, the last value is taken as the result of this fixed- χ calculation. Second, χ is multiplied by 2 and the previous procedure repeated until the resulting values differ by less than the small threshold 10^{-8} or χ is larger than 128. The second error is then the change between the value at the last fixed χ and the second-to-last calculation at fixed χ . The error is the larger of the first and second error. In our experience, this is a very conservative error measure which is likely to overestimate the error of the obtained value. Absent a better error estimation method, we will however use it in the following figures.

While the variational update is not yet implemented, its improvements are orthogonal to those discussed here, so we expect all results to carry over from imaginary time evolution to the variational update with minimal modifications. The same applies to the new extrapolation schemes for observables [29, 44].

Additionally, we should differentiate this tensor-based approach to global symmetries from an alternative in which one first parametrises all (e.g.) $SU(2)$ invariant tensors with a specific bond dimension and specific quantum numbers on each bond. In this alternative approach, one then works with dense state tensors (with complicated parametrised entries, which are optimised) but the symmetries do not necessarily extend to (e.g.) the environment tensors. This approach is in particular useful if the obtainable bond dimension is relatively small, as one may categorise and understand each individual state at a specific bond dimension and the relative advantage of a symmetry implementation at very small bond dimensions is also small.

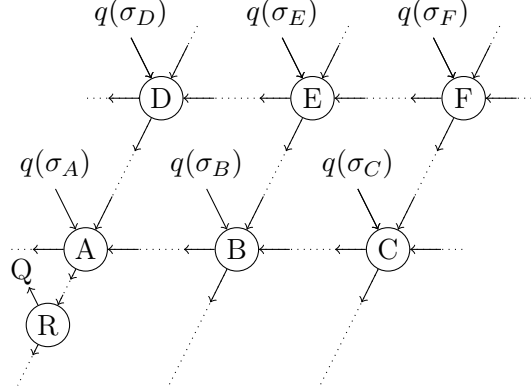


Figure 1: Layout of an example 2×3 iPEPS unit cell as used here. Each of the individual site tensors A, B, C, D, E and F inserts some charge into the network (which also depends on the local state), the special remover tensor R is used to extract a total charge Q from the unit cell. Auxiliary leg contractions are indicated by the dotted lines. The average quantum number on the inter-unit-cell auxiliary legs is zero (with some fluctuations) whereas intra-unit-cell legs can have non-zero average quantum number depending on the values of $q(\sigma)$ and the “routing” of charges through the unit cell.

3.1 Required adaptations of the iPEPS setup

The first step to combine symmetry-preserving tensors with an established tensor network algorithm is to define a consistent leg direction such that the tensor contractions required to, for example, represent the state are well-defined. The specific leg directions are entirely arbitrary, but of course have to be consistent within a calculation.¹

Second, when enforcing the symmetry, we effectively work in a canonical ensemble of a fixed average quantum number per unit cell. If this average quantum number is non-zero (e.g. 1 particle per site in the Hubbard model), it shifts the outgoing auxiliary tensor legs relative to the incoming auxiliary tensor legs. To account for this shift and give an overall consistent state, we insert an additional rank-3 *remover* tensor on the boundary of each unit cell. The remover tensor has a “physical” leg which points in the opposite direction of the usual physical legs on our iPEPS sites and simply removes as many particles as desired from the calculation. The additional leg is traced out during all calculations, for abelian symmetries, it amounts to an additional shift of the quantum numbers in each unit cell. The remover tensor is initialised as a random tensor with the required quantum number sectors on its three legs and then optimised during the iPEPS update of its two neighbouring sites.

Third, when constructing a single-site operator such as \hat{s}^+ in a $U(1)$ - S^z preserving system, it is necessary to insert an additional tensor leg to carry the additional quantum number. In the product $\hat{s}_i^+ \hat{s}_j^-$, these legs then combine to form a two-site gate acting on sites i and j connected by the contracted leg. If the contracted leg crosses any other tensor legs, the usual rule for fermionic PEPS applies [21] and a swap gate has to be inserted [22]. This swap gate fulfills the same role as Jordan-Wigner strings between operators \hat{c}^\dagger and \hat{c} in matrix-product operators [46].

¹Even when not enforcing the symmetry at the tensor level, a consistent choice of directions is required, as observed e.g. in Ref. [45].

3.2 Performance and accuracy necessitated by iPEPS compared to MPS

In a typical MPS-DMRG calculation, the maximal ranks of temporary tensors is typically limited to four or five, with the basic state building blocks having rank three. This has two beneficial side effects: first, the number of blocks in a tensor is limited to approximately $O(1000)$ with each individual block being relatively large. Second, the entries of the CGC tensors are regularly constructed from rank-2 and rank-3 tensors, which helps alleviate the buildup of numerical errors due to limited accuracy.

In an iPEPS calculation, in contrast, the maximal tensor ranks are much larger (rank 10 or above!), naively leading to tensors with $O(10^6)$ or more blocks. Furthermore, numerical errors in the CGC tensors build up very quickly as the basic rank-5 tensors already display a complicated Clebsch-Gordan structure.

The first issue is solely a performance problem and can be avoided by minimising tensor ranks wherever possible. In particular, it turns out that first constructing the rank-4 double-layer tensors and then applying the CTM algorithm based on the rank-4 tensors is effectively computationally more efficient than contracting the single-layer rank-5 tensors individually into the existing CTM tensors, even though the latter approach is asymptotically cheaper. However, the former decreases the overhead both from bookkeeping the tensors and initialising many extremely small matrix-matrix products. As iPEPS bond dimensions D are typically relatively small, argument about asymptotic efficiency also carry less weight than in (e.g.) MPS methods.

The second problem is more intricate and delayed by three tricks: First, we use higher-precision floating point numbers² to represent the entries of the CGC tensors. Second, within a tensor, we regularly check all non-zero coefficients (of which there are typically very few) and set those coefficients which are close in magnitude equal to each other. As an illustrative example, if a CGC tensor contains coefficients $[0.99, 1.01, -1.01, 0.99]$, we set them to $[1.00, 1.00, -1.00, 1.00]$. The actual closeness threshold used is $\approx 10^{-16}$. This relies on the fact that the coefficients of a CGC tensor are computed from very few inputs in very specific ways and no (typical) CGC tensor should truly contain coefficients different from each other but closer than 10^{-16} . Finally, it is helpful to regularly reconstruct the CGC tensors from scratch to remove all numerically buildup errors. This is done by first merging all tensor legs of the tensor until one arrives at a tensor with a single incoming and a single outgoing leg. In this tensor, the CGC tensors should be proportional to identity matrices which is then ensured manually. Afterwards, the tensor legs are split again to rebuild the original tensor structure.

An alternative solution for the issue of numerical accuracy would be to use continued fractions to represent the CGC coefficients to high accuracy as suggested in Ref. [30, 39] at the cost of a higher effort to implementation.

With these relatively minor changes, it becomes possible to do SU(2)- and U(1)-symmetric calculations on infinite projected entangled pair states using symmetric tensors in place of standard dense tensors without internal structure.

²Specifically, the `boost::multiprecision::cpp_bin_float<76>` type is used.

4 Computational speed-up

In classical DMRG calculations, implementing an abelian $U(1)$ symmetry typically leads to an approximately ten-fold computational speed-up or, alternatively, an approximately tripled bond dimension. Changing from a $U(1)$ to a $SU(2)$ symmetry has a similar effect of approximately tripling the effective bond dimension. To test the effect of the implemented symmetries, we pick two example systems, namely $S = 1/2$ spins on the Kagomé and square lattice.

4.1 Spin- $1/2$ square lattice Heisenberg model

As a first example, we consider the $S = 1/2$ Heisenberg Hamiltonian on a square lattice at the Heisenberg point of isotropic coupling:

$$\hat{H} = \sum_{\langle i,j \rangle} \hat{s}_i^x \hat{s}_j^x + \hat{s}_i^y \hat{s}_j^y + \hat{s}_i^z \hat{s}_j^z \quad . \quad (10)$$

The system spontaneously breaks the $SU(2)$ symmetry of the Hamiltonian but preserves both the \mathbb{Z}_2 and $U(1)$ - S^z symmetries.

The computational speed-up obtainable is first estimated by measuring the time required to re-initialise the corner transfer matrix with eight steps in each direction, evaluate the energy (evaluating eight two-site expectation values) and then do five full updates for imaginary time evolution of a second-order Trotter decomposition on a 2×2 unit cell. Each step requires the application of 16 gates. 8 of the 16 gates connect two neighbouring unit cells and hence also require a directional (up/down or left/right) CTM step. The runtime measurement is done after sufficiently many initial steps that the iPEPS bond dimension d and the bond dimension χ of the environment has saturated. For abelian (or no) symmetries, we set $\chi = 10(d + 1)$, while for the non-abelian $SU(2)$ case, $\chi = 5(d + 1)$ appears to be enough to obtain stability and convergence.

Fig. 2 shows the CPU time in seconds for the above procedure. These measurements were done on a single core of a Intel Xeon CPU E5-2630 v4 clocked at 2.20GHz. Except at minimal bond dimension $D = 2$, enforcing the $U(1)$ or \mathbb{Z}_2 symmetry has a very beneficial effect on the runtime. At larger bond dimensions, the $U(1)$ -symmetric calculation is also much faster than the \mathbb{Z}_2 -symmetric calculation. Comparing the reduced bond dimension d of a $SU(2)$ -symmetric calculation, one observes a very large cost (e.g. at $d = 3$: 89, 22, 12 and 653 seconds respectively without symmetries, with \mathbb{Z}_2 , $U(1)$ and $SU(2)$). Part of this large cost is due to a relatively large overhead of the CGC tensors, but another part comes from intermediate tensors (e.g. the rank-4 double layer tensors) having a larger relative bond dimension which is less amenable to a reduction in size by the symmetry implementation. On the other hand, when comparing the total effective bond dimension D , the $SU(2)$ -symmetric implementation is always faster (at $D = 4, 8, 12$) than a comparable calculation without this symmetry. Due to the model spontaneously breaking the $SU(2)$ symmetry in the ground state the obtained energies are not comparable and the data is included here only for completeness.

The error in energy per spin with and without symmetries is given in Fig. 3 relative to the reference value $E_0 \equiv -0.669437$ [47]. The calculation is initialised in a Néel state ($D = 1$) or (for the $SU(2)$ case) two singlets ($D = 2$) and then proceeds in stages. We first increase

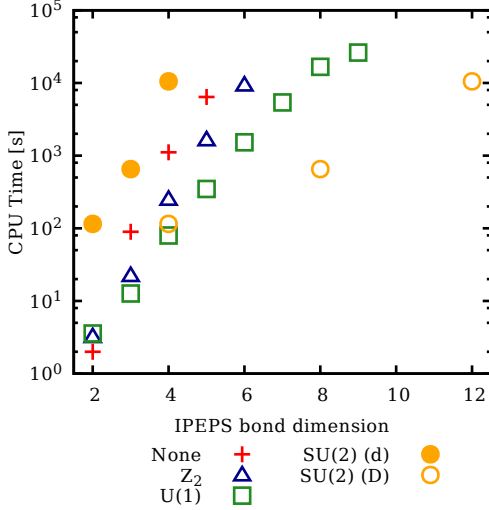


Figure 2: Computational effort for CTM initialisation, energy evaluation and five FFU steps in imaginary time in the Heisenberg square lattice model. Data for the SU(2)-symmetric calculation is plotted over the reduced (d) and total (D) bond dimension.

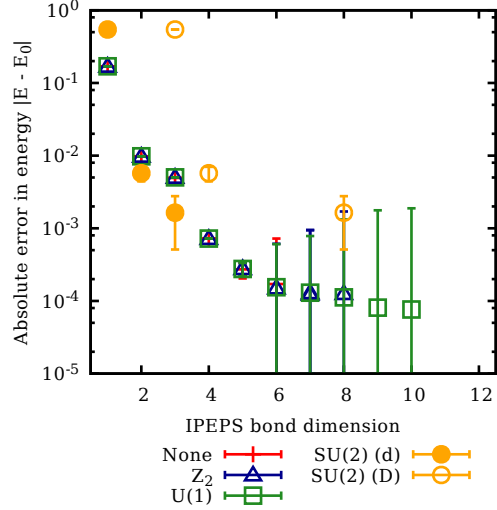


Figure 3: Error in energy per spin calculated in the Heisenberg square lattice model at $\Delta = 1$ with $E_0 = -0.669437$. Error bars are obtained from the CTM calculation and give the error of the observable relative to its true value in the given variational state.

the bond dimension to $d = 2$ and then time evolve with step size $\delta\tau = 1, 0.1, 0.01$ until the energy (estimated every five steps) stops decreasing. Subsequently, we either decrease $\delta\tau$ or, if we reached the minimal specified $\delta\tau$, increase d and reset $\delta\tau$ to a larger value (0.1). Starting at $d = 3$, we allow a smaller minimal $\delta\tau = 0.001$. The Trotter error should hence be of order $O(\delta\tau^2) \approx 10^{-6}$. The energy estimates during the time evolution are at a fixed χ and with a re-initialised environment to trade-off accuracy and computational effort. Each obtained state is however also saved to disk.

The expectation values shown are then evaluated on the stored states as described in Sec. 3, in particular, error bars estimate the error of the calculated value compared to the true value of the given state. Due to our maximal environment bond dimension being limited to $\chi = 128$, error bars become relatively large in the logarithmic plot. Data for SU(2) is only included for completeness, so let us focus on the three other curves for calculations with no symmetries, \mathbb{Z}_2 symmetry and U(1) symmetry:

Contrary to Ref. [36] but in agreement with Refs. [37, 40] we find very comparable results with and without symmetries at identical bond dimensions. In particular at larger bond dimensions ($D = 5, 6$), enforcing the symmetry appears to aid the calculation as we can guide the state into the correct sector. This difference is most likely an effect of the fixed quantum number distribution with an equal number of states per sector used in Ref. [36] which reduces the expressive power of the state.

As expected, growing computational effort makes calculations at larger D only accessible with the full U(1) symmetry. In addition to the reduced matrix sizes, the blocking of tensors also allows for a straightforward shared-memory parallelisation which was used here to obtain converged $D \geq 7$ results at acceptable wallclock times of no more than two days. For these larger bond dimensions, we observe that the obtained error gradually ceases to shrink. We

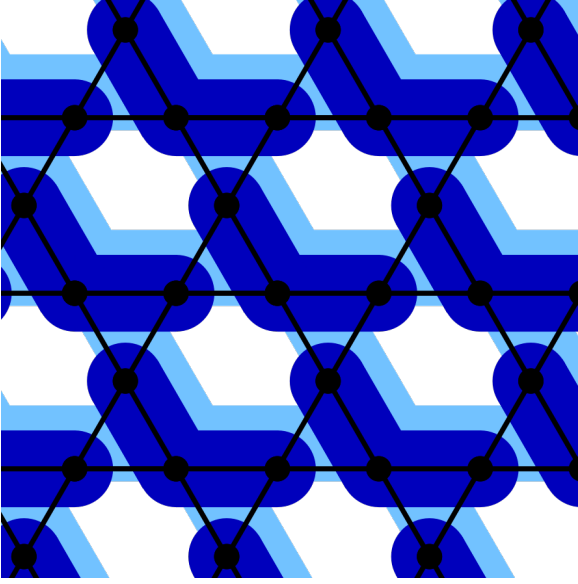


Figure 4: The mapping of the Kagomé lattice to the square lattice used here. Three sites of the Kagomé lattice (black circles) are merged into one site of the square lattice (dark blue). Each link between two square-lattice sites (light blue) corresponds to two links of the Kagomé lattice (black lines).

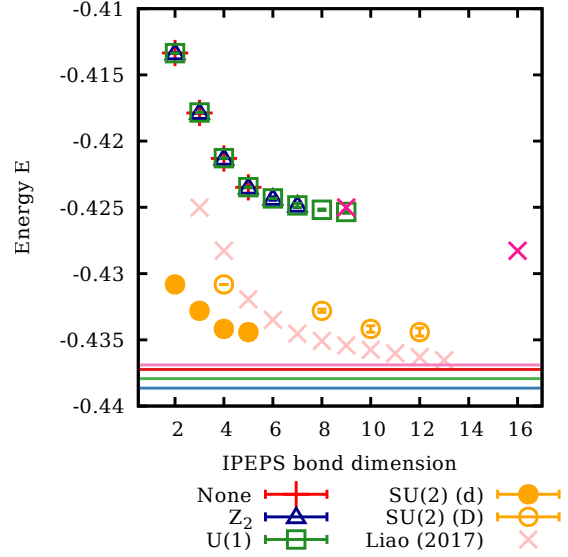


Figure 5: Ground state energy per spin on the Kagomé lattice. The square lattice mapping leads to energies which are considerably worse than the current best estimates $E_0 \approx -0.437$ (values from [50], [51], [52], [17] shown as lines in top-down order, 9-site PESS from Ref. [51] as pink crosses).

expect that a variational update of the tensors should decrease the energy further.

4.2 The Kagomé lattice

While the Heisenberg Hamiltonian on the Kagomé lattice is the subject of ongoing research (e.g. cf. Refs. [17, 48–52]), here, we only wish to benchmark the effect of a $SU(2)$ spin symmetry which is probably not spontaneously broken in the ground state. Our implementation currently only handles square lattices, requiring a mapping of the Kagomé lattice to the square lattice (cf. Fig. 4 and e.g. Ref. [49]). This mapping is exact, the resulting 8-dimensional space of the square lattice sites is not truncated.³ However, the mapping is not optimal as two links in the Kagomé lattice are represented by just a single link in the square lattice, which then requires an approximately squared bond dimension to represent the same amount of entanglement. This difficulty should affect the calculations with and without symmetries mostly in the same way and hence does not preclude an analysis of the effect of the symmetry implementation here. A smarter approach is to adapt the structure of the tensor network to the Kagomé lattice and potentially introducing additional tensors to aid in convergence [49–51].

Earlier work [50, 51] has found a ground state energy of approximately -0.437 using iPEPS calculations with the simple update mechanism. DMRG calculations on cylinders extrapolated to the 2D thermodynamic limit resulted in ground state energies per spin of $-0.4386(5)$ [17] if

³One could, of course, consider such a truncation in future works, e.g. excluding the high-spin states $S = 3/2$ completely from the calculation.

SU(2) symmetry was conserved and $-0.4379(3)$ without conservation of SU(2) symmetry [52] and subsequently a smaller effective bond dimension.

Fig. 5 shows the results for the energy per spin with and without symmetries for our implementation. The figure also includes reference values as follows: first, solid lines show the extrapolated, final values from Ref. [50], [51], [52] and [17] (in top-down order); the first two are iPEPS calculations whereas the latter two are DMRG calculations on cylinders extrapolated to the thermodynamic limit. Second, light pink crosses reproduce the 9-site PESS data in Ref. [51]. Third, the two bright pink crosses on the right-hand side show the same data, but for an effectively squared bond dimension as Ref. [51] does not use the square lattice mapping.

Calculations with no symmetries, \mathbb{Z}_2 symmetry and U(1) symmetry obtain essentially identical results with the only difference being a drastic computational speed-up allowing $D = 5$ without symmetries but $D = 9$ with U(1) symmetry. This is expected and fully in-line with calculations on the square lattice above. Given our mapping of the Kagomé to the square lattice, also the difference between the results here and earlier works is not too worrisome. Even a certain degree of continuity between our data and the data from Ref. [51] plotted over the squared bond dimension (bright pink crosses) is visible. As the square lattice bonds need to transport approximately twice as much entanglement as the Kagomé lattice bonds in Ref. [51], this is also expected.

The comparison with the SU(2)-invariant calculation (yellow circles in Fig. 5) is more interesting: Comparing both reduced and total bond dimensions, we obtain substantially lower energies with SU(2)-invariant tensors than without. While the former is to be expected, the latter is surprising: Given two tensors of the same total bond dimension D , both are able to represent the same state and hence can be used to construct states with identical energies.

Instead, the update procedure used here (fast full update) and its associated convergence problems must be responsible for the drastic difference in energies: it appears to be much easier to obtain a low-energy state using SU(2)-invariant tensors than using unconstrained tensors. Multiple effects likely contribute: first, the initial random state with SU(2) invariance is typically a much better ground-state candidate than a random state which is not SU(2) invariant. In the latter case, the imaginary time evolution first has to rebuild the SU(2) invariance of the state from an initially symmetry-broken state. Second, during this reconstruction, the truncation of the state is not guaranteed to preserve its (attempt at) SU(2) invariance. Instead, degenerate multiplets may be truncated in the middle to obtain the target bond dimension. Third, while the gauge fixing mechanism used here greatly improves the accuracy and efficiency of the calculation, it is still not perfect and large bond dimensions may still lead to relatively large condition numbers of the norm tensors. By only considering smaller reduced tensors, this problem is avoided longer in the SU(2) invariant calculation.

4.3 Summary for the computational speed-up

In this section, we presented results showing that by implementing either abelian or non-abelian symmetries, larger bond dimensions and hence better results are obtainable at comparable computational effort. In the Heisenberg model, $d = 10$ is possible when implementing the U(1) symmetry, which approximately doubles the bond dimension compared to our best calculations without any symmetries. As expected, the \mathbb{Z}_2 symmetry provides a smaller benefit than the U(1) symmetry but still a noticeable speed-up. In the Kagomé model, implementing the SU(2) symmetry leads to much faster convergence and hence much better results compared to calculations without symmetries.

We must stress that these are “merely” practical advantages: given a sufficiently fast computer, there is no computational benefit in implementing a symmetry into a tensor network. However, we will show in the next section that implementing or not implementing a symmetry provides an additional control which can be used to obtain qualitatively different results.

5 Diagnosing spontaneous symmetry breaking

Implementing a symmetry in a system not only allows for a potential computational speed-up, but also provides additional measures to control the calculation.

First, forcing a state to transform uniquely under a symmetry is equivalent to doing the calculation in a canonical instead of grand-canonical ensemble. As a result, it becomes possible to fix total particle number (or average particle number per unit cell) exactly to a desired value. For example in the Kagomé calculation, the states with $SU(2)$ symmetry are exact eigenstates of the total spin operator with eigenvalue $S \equiv 0$ and the states with $U(1)$ symmetry are exact eigenstates of the total \hat{S}^z operator with eigenvalue $S^z \equiv 0$. In contrast, the states without any symmetry only have $S^z \approx 0$. It then becomes possible to e.g. exactly fix the total particle number per unit cell in the Hubbard model instead of relying on a chemical potential to obtain the desired filling fraction. On the flip side, filling fraction and unit cell size have to be commensurate to provide an integer average particle number per unit cell. This integer average particle number is removed by the “remover” tensor described in Sec. 3.1 and Fig. 1.

Second, symmetry-preserving tensors can only represent eigenstates of the symmetry. If the symmetry operator and the Hamiltonian commute and are non-degenerate, each eigenstate of the Hamiltonian is also an eigenstate of the symmetry operator and this is no restriction. If, however, the Hamiltonian has a degenerate spectrum, eigenstates of the Hamiltonian are not necessarily eigenstates of the symmetry operator. Then optimising eigenstates of the symmetry operator for the lowest energy does not yield a natural eigenstate of the Hamiltonian but instead some superposition of degenerate eigenstates. Such superpositions have typically larger entanglement, or, if we fix the maximal entanglement, a higher energy than if we allowed breaking of the symmetry in the ansatz.

The increased entanglement of symmetric superpositions can be used to diagnose spontaneous symmetry breaking: If a symmetry is not broken, then it should be possible to implement this symmetry in the tensor network. The resulting state should be an equally good candidate to represent the ground state as a state constructed from unrestricted tensors. As such, at a fixed bond dimension, we expect to find the same variational energy regardless of whether we implement an abelian symmetry or not provided that there are no problems with convergence and the symmetry sectors are chosen in an optimal fashion. Non-abelian symmetries are more tricky, as they increase the effective bond dimension of the state and hence lead to more difficult comparisons. If, on the other hand, a symmetry is spontaneously broken, we expect a better variational energy if we also allow the tensors in our tensor network state to break this symmetry. For lack of spontaneous symmetry breaking in finite and also one-dimensional infinite systems, this is not a problem often encountered. In iPEPS calculations, however, it does become relevant.

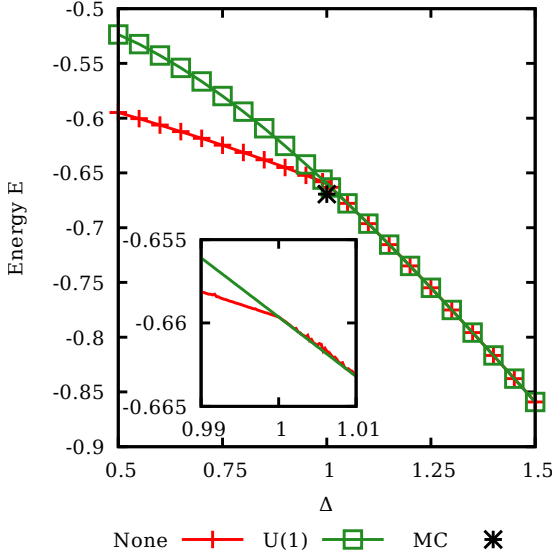


Figure 6: Obtainable ground-state energies in the anisotropic Heisenberg model at $D = 2$ with and without U(1) symmetry. Inset: Zoom into the central region, Δ values are placed 0.0025 apart. Lines are guides to the eye. The results start to differ at $\Delta < 1$.

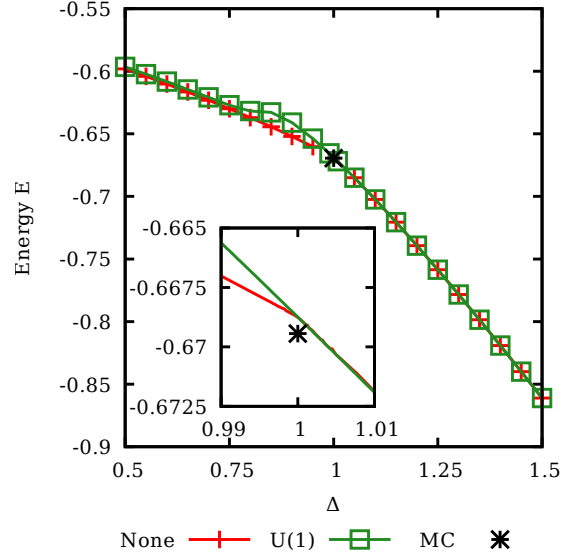


Figure 7: As left, for $D = 4$. At small enough Δ , the U(1) symmetric state becomes competitive again but still has slightly higher energy than the unconstrained state. Monte Carlo reference value at $\Delta = 1$ taken from Ref. [47]. Error bars are smaller than symbol size in all cases.

The Heisenberg model on the square lattice as discussed before can serve as an example of this effect. The Hamiltonian is:

$$\hat{H} = \sum_{\langle i,j \rangle} \hat{s}_i^x \hat{s}_j^x + \hat{s}_i^y \hat{s}_j^y + |\Delta| \hat{s}_i^z \hat{s}_j^z \quad . \quad (11)$$

with now Δ not fixed at 1. At $\Delta < 1$, the ground state spontaneously breaks the U(1)- S^z symmetry and only keeps a canted order. If, for a fixed and finite bond dimension D , we then plot the optimal energy obtained over the value of Δ for different calculations with and without that symmetry, we can straightforwardly diagnose the transition point, cf. Figs. 6 and 7. Here, we only need to measure the energy of the system – a local observable which is straightforward to evaluate with reliable error bars. More importantly, states are optimised for their energy. The energy is hence typically the observable which behaves in the most stable manner and most closely represents the value obtained in an actual physical state. By comparing the behaviour of the different calculations over the transition point at $\Delta = 1$, we can easily conclude that the U(1)- S^z symmetry is spontaneously broken at $\Delta < 1$ due to the considerably lower energy obtained from an unconstrained calculation.

Furthermore, while a clear kink at $\Delta = 1$ is visible in the energy in calculations without symmetry, this kink is absent and the energy a nearly linear function of Δ around $\Delta = 1$ in the calculation with U(1) symmetry. The strong bias towards a symmetry-unbroken state completely hides the symmetry-broken phase from the U(1)-symmetric calculation. Hence, by implementing a symmetry in a system, we can not only select a sector in which we want to do

our calculation (e.g. $S^z = 0$ or $N/L = 0.5$) but also – to some extent – select the symmetries present in the calculated states. Of course, at arbitrarily large D , it becomes possible for the calculation to hide the symmetry-breaking by a suitable superposition as discussed before. This effect can be seen at $\Delta < 0.8$ and $D \geq 4$, where the U(1)-symmetric calculation is again somewhat comparable to the unsymmetric calculation.

If we implement the \mathbb{Z}_2 symmetry, we disallow unit cell states with $S^z = \pm 1$, on the 2×2 unit cell in a vacuum environment this hence limits us to the two ferromagnetic states (which are very highly energetic and don't play a role) and the six $S^z = 0$ states. With a suitable environment, one could alleviate this problem by combining a $S^z = 1$ state from the environment with a local $S^z = -1$. However, introducing such a state would break the U(1) symmetry (as it should), which is *preserved by the Hamiltonian we use for the evolution*.

Put another way, starting from an antiferromagnetic state $|\psi\rangle$ with $S^z = 0$, the global ground state is not contained in the Krylov subspace of \hat{H} and $|\psi\rangle$. As such, it is not possible to obtain it by imaginary time evolution alone. Worse, if we initialise the evolution with a symmetry-broken state (of comparatively high energy), the symmetry-broken contribution to this state is very quickly removed by the automatic truncation and hence not available when it would be useful to lower the energy. This problem is not limited to calculations with \mathbb{Z}_2 symmetry. Also for calculations without any symmetries, it was necessary to select multiple random initial states and run the calculation at $D = 2$ multiple times to obtain the correct ground-state energy. Initialising the calculation without symmetries with a Néel state resulted in energies typically very close to those obtained from the calculation with full U(1) symmetry. Only very rarely have we found the error from the truncation to lead to spontaneous symmetry breaking by itself.

Avenues to avoid this problem could be random noise terms added to the state or special “tunneling” Hamiltonians (e.g. $\hat{s}^+ \hat{s}^+ + \hat{s}^- \hat{s}^-$) which are added to the Hamiltonian with a small prefactor and allow for tunneling between different symmetry sectors. The latter approach is already fairly common when solving complicated systems using DMRG. This, however, is outside the scope of the present paper.

6 Conclusion

We have shown a considerable computational advantage to be derived from the implementation of symmetries in iPEPS tensor networks. For example implementing a U(1)- S^z symmetry in the Heisenberg square lattice model allows for a maximal bond dimension $D = 10$ at effort comparable to a calculation without any symmetries at $D = 6$. Furthermore, we show that the explicit Clebsch-Gordan Coefficient approach is sufficient to represent SU(2)-symmetric tensors and provides for a large advantage in the Kagomé Heisenberg model. Finally, we provide an example of how implementing a symmetry allows for further control of the calculation by firstly either enabling or disabling the symmetry itself and secondly selecting the desired quantum number sector if the symmetry is enabled.

Acknowledgements

We are thankful for very helpful discussions with I. P. McCulloch, M. C. Bañuls, J. I. Cirac, L. Vanderstraten, F. Verstraete and N. Schuch. We also much appreciated comments by E. M. Stoudenmire on the first version of this paper.

Funding information Funding through ERC Grant QUENOCOBA, ERC-2016-ADG (Grant no. 742102) is acknowledged.

References

- [1] U. Schollwöck, *The density-matrix renormalization group in the age of matrix product states*, Ann. Phys. **326**(1), 96 (2011), doi:10.1016/j.aop.2010.09.012.
- [2] Y.-Y. Shi, L.-M. Duan and G. Vidal, *Classical simulation of quantum many-body systems with a tree tensor network*, Phys. Rev. A **74**, 022320 (2006), doi:10.1103/PhysRevA.74.022320.
- [3] V. Murg, F. Verstraete, O. Legeza and R. M. Noack, *Simulating strongly correlated quantum systems with tree tensor networks*, Phys. Rev. B **82**, 205105 (2010), doi:10.1103/PhysRevB.82.205105.
- [4] L. Tagliacozzo, G. Evenbly and G. Vidal, *Simulation of two-dimensional quantum systems using a tree tensor network that exploits the entropic area law*, Phys. Rev. B **80**, 235127 (2009), doi:10.1103/PhysRevB.80.235127.
- [5] M. Gerster, P. Silvi, M. Rizzi, R. Fazio, T. Calarco and S. Montangero, *Unconstrained tree tensor network: An adaptive gauge picture for enhanced performance*, Phys. Rev. B **90**, 125154 (2014), doi:10.1103/PhysRevB.90.125154.
- [6] K. Gunst, F. Verstraete, S. Wouters, O. Legeza and D. Van Neck, *T3NS: Three-legged tree tensor network states*, Journal of Chemical Theory and Computation **14**(4), 2026 (2018), doi:10.1021/acs.jctc.8b00098.
- [7] D. Bauernfeind, M. Zingl, R. Triebl, M. Aichhorn and H. G. Evertz, *Fork tensor-product states: Efficient multiorbital real-time DMFT solver*, Phys. Rev. X **7**, 031013 (2017), doi:10.1103/PhysRevX.7.031013.
- [8] F. A. Wolf, A. Go, I. P. McCulloch, A. J. Millis and U. Schollwöck, *Imaginary-time matrix product state impurity solver for dynamical mean-field theory*, Phys. Rev. X **5**, 041032 (2015), doi:10.1103/PhysRevX.5.041032.
- [9] K. M. Stadler, Z. P. Yin, J. von Delft, G. Kotliar and A. Weichselbaum, *Dynamical mean-field theory plus numerical renormalization-group study of spin-orbital separation in a three-band Hund metal*, Phys. Rev. Lett. **115**, 136401 (2015), doi:10.1103/PhysRevLett.115.136401.

- [10] G. Knizia and G. K.-L. Chan, *Density matrix embedding: A simple alternative to dynamical mean-field theory*, Phys. Rev. Lett. **109**, 186404 (2012), doi:10.1103/PhysRevLett.109.186404.
- [11] G. Knizia and G. K.-L. Chan, *Density matrix embedding: A strong-coupling quantum embedding theory*, J. Chem. Theory Comput. **9**(3), 1428 (2013), doi:10.1021/ct301044e.
- [12] B.-X. Zheng, C.-M. Chung, P. Corboz, G. Ehlers, M.-P. Qin, R. M. Noack, H. Shi, S. R. White, S. Zhang and G. K.-L. Chan, *Stripe order in the underdoped region of the two-dimensional Hubbard model*, Science **358**(6367), 1155 (2017), doi:10.1126/science.aam7127, <http://science.sciencemag.org/content/358/6367/1155.full.pdf>.
- [13] Y. Deng, E. Kozik, N. V. Prokof'ev and B. V. Svistunov, *Emergent BCS regime of the two-dimensional fermionic Hubbard model: Ground-state phase diagram*, EPL **110**(5), 57001 (2015), doi:10.1209/0295-5075/110/57001.
- [14] E. Stoudenmire and S. R. White, *Studying two-dimensional systems with the density matrix renormalization group*, Annu. Rev. Condens. Matter Phys. **3**(1), 111 (2012), doi:10.1146/annurev-conmatphys-020911-125018.
- [15] J. P. F. LeBlanc, A. E. Antipov, F. Becca, I. W. Bulik, G. K.-L. Chan, C.-M. Chung, Y. Deng, M. Ferrero, T. M. Henderson, C. A. Jiménez-Hoyos, E. Kozik, X.-W. Liu *et al.*, *Solutions of the two-dimensional Hubbard model: Benchmarks and results from a wide range of numerical algorithms*, Phys. Rev. X **5**, 041041 (2015), doi:10.1103/PhysRevX.5.041041.
- [16] G. Ehlers, S. R. White and R. M. Noack, *Hybrid-space density matrix renormalization group study of the doped two-dimensional Hubbard model*, Phys. Rev. B **95**, 125125 (2017), doi:10.1103/PhysRevB.95.125125.
- [17] S. Depenbrock, I. P. McCulloch and U. Schollwöck, *Nature of the spin-liquid ground state of the $S = 1/2$ Heisenberg model on the Kagome lattice*, Phys. Rev. Lett. **109**, 067201 (2012), doi:10.1103/PhysRevLett.109.067201.
- [18] F. Verstraete and J. I. Cirac, *Renormalization algorithms for quantum-many body systems in two and higher dimensions* (2004), [cond-mat/0407066](https://arxiv.org/abs/cond-mat/0407066).
- [19] F. Verstraete, V. Murg and J. Cirac, *Matrix product states, projected entangled pair states, and variational renormalization group methods for quantum spin systems*, Advances in Physics **57**(2), 143 (2008), doi:10.1080/14789940801912366, <https://doi.org/10.1080/14789940801912366>.
- [20] J. Jordan, R. Orús, G. Vidal, F. Verstraete and J. I. Cirac, *Classical simulation of infinite-size quantum lattice systems in two spatial dimensions*, Phys. Rev. Lett. **101**, 250602 (2008), doi:10.1103/PhysRevLett.101.250602.
- [21] P. Corboz, R. Orús, B. Bauer and G. Vidal, *Simulation of strongly correlated fermions in two spatial dimensions with fermionic projected entangled-pair states*, Phys. Rev. B **81**, 165104 (2010), doi:10.1103/PhysRevB.81.165104.

- [22] P. Corboz, J. Jordan and G. Vidal, *Simulation of fermionic lattice models in two dimensions with projected entangled-pair states: Next-nearest neighbor hamiltonians*, Phys. Rev. B **82**, 245119 (2010), doi:10.1103/PhysRevB.82.245119.
- [23] P. Corboz, T. M. Rice and M. Troyer, *Competing states in the t - J model: Uniform d -wave state versus stripe state: supplemental material*, Phys. Rev. Lett. **113**, 046402 (2014), doi:10.1103/PhysRevLett.113.046402.
- [24] M. Lubasch, J. I. Cirac and M.-C. Bañuls, *Algorithms for finite projected entangled pair states*, Phys. Rev. B **90**, 064425 (2014), doi:10.1103/PhysRevB.90.064425.
- [25] H. N. Phien, I. P. McCulloch and G. Vidal, *Fast convergence of imaginary time evolution tensor network algorithms by recycling the environment*, Phys. Rev. B **91**, 115137 (2015), doi:10.1103/PhysRevB.91.115137.
- [26] H. N. Phien, J. A. Bengua, H. D. Tuan, P. Corboz and R. Orús, *Infinite projected entangled pair states algorithm improved: Fast full update and gauge fixing*, Phys. Rev. B **92**, 035142 (2015), doi:10.1103/PhysRevB.92.035142.
- [27] L. Vanderstraeten, J. Haegeman, P. Corboz and F. Verstraete, *Gradient methods for variational optimization of projected entangled-pair states*, Phys. Rev. B **94**, 155123 (2016), doi:10.1103/PhysRevB.94.155123.
- [28] P. Corboz, *Variational optimization with infinite projected entangled-pair states*, Phys. Rev. B **94**, 035133 (2016), doi:10.1103/PhysRevB.94.035133.
- [29] P. Corboz, *Improved energy extrapolation with infinite projected entangled-pair states applied to the two-dimensional Hubbard model*, Phys. Rev. B **93**, 045116 (2016), doi:10.1103/PhysRevB.93.045116.
- [30] A. Weichselbaum, *Non-abelian symmetries in tensor networks: A quantum symmetry space approach*, Ann. Phys. **327**(12), 2972 (2012), doi:10.1016/j.aop.2012.07.009.
- [31] J. Hauschild, R. S. K. Mong, F. Pollmann, M. Schulz, L. Schoonderwoert, J. Unfried, Y.-C. Tzeng and M. P. Zaletel, *Tensor Network Python (TENPY)*.
- [32] I. P. McCulloch, *The matrix product toolkit*, MPS/DMRG Software Suite.
- [33] E. M. Stoudenmire, S. R. White and The ITensor Collaboration, *ITENSOR C++ library*.
- [34] I. P. McCulloch and M. Gulácsi, *The non-abelian density matrix renormalization group algorithm*, EPL **57**(6), 852 (2002), doi:10.1209/epl/i2002-00393-0.
- [35] S. Singh and G. Vidal, *Tensor network states and algorithms in the presence of a global $SU(2)$ symmetry*, Phys. Rev. B **86**, 195114 (2012), doi:10.1103/PhysRevB.86.195114.
- [36] B. Bauer, P. Corboz, R. Orús and M. Troyer, *Implementing global abelian symmetries in projected entangled-pair state algorithms*, Phys. Rev. B **83**, 125106 (2011), doi:10.1103/PhysRevB.83.125106.
- [37] R. Haghshenas and D. N. Sheng, *$U(1)$ -symmetric infinite projected entangled-pair states study of the spin-1/2 square J_1 - J_2 Heisenberg model*, Phys. Rev. B **97**, 174408 (2018), doi:10.1103/PhysRevB.97.174408.

- [38] S. Singh, R. N. C. Pfeifer and G. Vidal, *Tensor network decompositions in the presence of a global symmetry*, Phys. Rev. A **82**, 050301 (2010), doi:10.1103/PhysRevA.82.050301.
- [39] B. Bruognolo, *Tensor network techniques for strongly correlated systems*, Ph.D. thesis, LMU Munich (2017).
- [40] T. Liu, W. Li, A. Weichselbaum, J. von Delft and G. Su, *Simplex valence-bond crystal in the spin-1 Kagome Heisenberg antiferromagnet*, Phys. Rev. B **91**, 060403 (2015), doi:10.1103/PhysRevB.91.060403.
- [41] C. Hubig, F. Lachenmaier, N.-O. Linden, T. Reinhard, L. Stenzel and A. Swoboda, *The SYTEN toolkit*.
- [42] C. Hubig, *Symmetry-Protected Tensor Networks*, Ph.D. thesis, LMU München (2017).
- [43] C. Hubig, I. P. McCulloch, U. Schollwöck and F. A. Wolf, *Strictly single-site DMRG algorithm with subspace expansion*, Phys. Rev. B **91**, 155115 (2015), doi:10.1103/PhysRevB.91.155115.
- [44] M. Rader and A. M. Läuchli, *Finite correlation length scaling in Lorentz-invariant gapless iPEPS wave functions* (2018), 1803.08566v1.
- [45] A. Hackenbroich, A. Sterdyniak and N. Schuch, *Interplay of $SU(2)$, point group, and translational symmetry for projected entangled pair states: Application to a chiral spin liquid*, Phys. Rev. B **98**, 085151 (2018), doi:10.1103/PhysRevB.98.085151.
- [46] C. Hubig, I. P. McCulloch and U. Schollwöck, *Generic construction of efficient matrix product operators*, Phys. Rev. B **95**, 035129 (2017), doi:10.1103/PhysRevB.95.035129.
- [47] A. W. Sandvik, *Finite-size scaling of the ground-state parameters of the two-dimensional Heisenberg model*, Phys. Rev. B **56**, 11678 (1997), doi:10.1103/PhysRevB.56.11678.
- [48] Y.-C. He, M. P. Zaletel, M. Oshikawa and F. Pollmann, *Signatures of Dirac cones in a DMRG study of the Kagome Heisenberg model*, Phys. Rev. X **7**, 031020 (2017), doi:10.1103/PhysRevX.7.031020.
- [49] P. Corboz, K. Penc, F. Mila and A. M. Läuchli, *Simplex solids in $SU(N)$ Heisenberg models on the kagome and checkerboard lattices*, Phys. Rev. B **86**, 041106 (2012), doi:10.1103/PhysRevB.86.041106.
- [50] J.-W. Mei, J.-Y. Chen, H. He and X.-G. Wen, *Gapped spin liquid with F_2 topological order for the Kagome Heisenberg model*, Phys. Rev. B **95**, 235107 (2017), doi:10.1103/PhysRevB.95.235107.
- [51] H. J. Liao, Z. Y. Xie, J. Chen, Z. Y. Liu, H. D. Xie, R. Z. Huang, B. Normand and T. Xiang, *Gapless spin-liquid ground state in the $S = 1/2$ Kagome antiferromagnet*, Phys. Rev. Lett. **118**, 137202 (2017), doi:10.1103/PhysRevLett.118.137202.
- [52] S. Yan, D. A. Huse and S. R. White, *Spin-liquid ground state of the $S = 1/2$ Kagome Heisenberg antiferromagnet*, Science **332**(6034), 1173 (2011), doi:10.1126/science.1201080.